IMPACT OF A DEAN VORTEX-CHARACTERIZED INFLOW STREAM ON THERMAL MIXING IN A T-JUNCTION: A SENSITIZED-RANS MODELING STUDY

Ivan Joksimović[1], **Tarik Čorbo**[2], **Suad Jakirlić**[1]
[1]Institute of Fluid Mechanics and Aerodynamics, Technical University Darmstadt
Allarich-Weiss Straße 10, 64287 Darmstadt, Germany
[2]Faculty of Mechanical Engineering, University of Sarajevo,
Vilsonovo setaliste 9, 71000 Sarajevo, Bosnia and Herzegovina
joksimovic@sla.tu-darmstadt.de, jakirlic@sla.tu-darmstadt.de

ABSTRACT

A computational study focusing on the thermal mixing of two fluid streams in a T-junction configuration investigated by Tunstall *et al.* (2016) has been presently performed by applying a RANS-based eddy-resolving model of turbulence. Main, low-temperature stream enters the T-junction at a Reynolds number corresponding to $Re = 107893$ after passing through a 90° bend. The secondary, high-temperature stream is injected perpendicularly into main branch at a Reynolds number of 5422. Substantial difference between flow rates of two streams causes formation of a characteristic mixing process resembling a re-attached jet configuration. Of particular interest is its interference with the secondary vortices - the so-called Dean vortices - that are convected from the curved main inlet, producing a low-rank mixing structures in its wake. The computational framework relying on the scale-adaptive turbulence modeling approach, introduced by Menter & Egorov (2010), has been used to simulate dynamics of large-scale turbulent structures with moderate spatial and temporal resolution requirements. The motion of unresolved sub-scale structures are described by an appropriately sensitized near-wall differential Reynolds-stress model according to Jakirlic & Maduta (2015).

INTRODUCTION

The study of momentum and heat exchange in the turbulent mixing processes involving two or more fluid streams of different temperatures within the pipelines of different geometric complexity is one of the core areas of fluid mechanics and thermodynamics. The performance capabilities and efficiency of relevant thermal-hydraulic equipment is based to the greatest extent on the understanding of the flow and thermodynamic processes and their interactions operating therein. Mixing processes in industrial pipeworks involve often high-Reynolds number flows characterized by complex associated phenomena such as spatially and temporally evolving structural flow dynamics, secondary currents and high level of turbulence anisotropy. This makes them extremely demanding for industry-scale simulations. Computationally more suitable RANS (Reynolds-Averaged Navier-Stokes) models are often incapable to properly capture flow anisotropy and highly unsteady flows dynamics, whereas the current LES (Large-Eddy Simulation) models require, despite their advantageous accuracy in resolving the major portion of underlying turbulence spectrum, enhanced computational resources at high Reynolds numbers. To overcome the above-mentioned problems, a recently proposed 'scale-adaptive' turbulence modeling strategy, Menter & Egorov (2010), has been applied on an industrially relevant moderately high Reynolds number case which involves mixing of two fluid streams with different temperatures. The dynamics of relevant sub-scales is modeled by an adequately sensitized anisotropy-resolving Reynolds-stress model. The model applied is capable of reproducing low-rank turbulent structures and their temporal dynamics at lower cost, comparing to the LES frameworks. The database originating from the experimental investigation by Hosseini *et al.* (2008) and detailed LES study by Tunstall *et al.* (2016) of the thermal mixing in a T-Junction configuration is adopted presently as a reference for computation and results comparison. Schematic of the computational domain with indicated boundaries is shown in Fig. 2. Configuration dimensions and operating parameters are listed in Table 1.

Table 1. Operating conditions

Parameters	Main line	Branch line
Diameter [mm]	108	21
Bulk velocity [m/s]	0.89	0.23
Reynolds number	107,893	5422
Temperature (dimensionless)	1	0

COMPUTATIONAL METHODOLOGY

Following the LES-reference, the incompressible flow conditions are assumed. The equation system comprising the continuity-, momentum- and temperature-evolution equations, as well as the equations governing the turbulent quantities, Reynolds stress components $\overline{u_i u_j}$ and the specific dissipation rate ω^h, is implemented into the open-source C++ Library OpenFOAM, with which all simulations have been performed. Simplified-gradient-hypothesis (SGH) has been applied for calculation of sub-grid heat fluxes since the dominant portion of fluctuating energy would be attained at resolved scales. Formally, second-order accurate schemes are applied for discretization of both temporal and spatial derivatives. Adaptive time stepping with the criterion $CFL < 0.7$ is used.

As previously stated, choice of adequate turbulence model, capable of accounting for the complex flow phenomena, represents a nontrivial task. Since the most energetic coherent structures in the flow are characterized by low-frequency dynamics, only a top-level portion of turbulent spectrum needs to be resolved, and the remaining part may be modeled. This relativizes the requirements for fine grid resolution. For that purpose, the 'eddy-resolving' version of differential Reynolds Stress Model (RSM) by Jakirlic & Hanjalic (2002), denoted as Instability-Sensitive RSM - IS-RSM, has been used. Detailed derivation and scrutiny of the model can be found in Jakirlic & Maduta (2015). Modeled turbulence is accounted for by the evolution equation for Reynolds Stress Tensor $\overline{u_i u_j}$, including the effects of production P_{ij}, dissipation ε_{ij}, redistribution Φ_{ij} and diffusion D_{ij}, with the latter consisting of molecular and turbulent diffusion.

$$\frac{D\overline{u_i u_j}}{Dt} = P_{ij} - \varepsilon_{ij} + \Phi_{ij} + D^t_{ij} + D^\nu_{ij} \tag{1}$$

The principal 'eddy-resolving' strategy behind the IS-RSM aiming at appropriately sensitizing the model is to introduce an additional production term P_{SAS} into the equation of the scale-supplying variable: $\omega^h = \varepsilon^h / k$, in line with the Scale-Adaptive Simulation (SAS) proposal by Menter & Egorov (2010).

$$\frac{D\omega^h}{Dt} = \left(\frac{D\omega^h}{Dt}\right)_{RANS} + P_{SAS} \tag{2}$$

By doing so, the correspondingly enhanced dissipation of modeled turbulent quantities suppresses their intensity towards the sub-scale level (not sub-grid scale level; the present model formulation is grid-spacing free). The turbulence production is shifted to the resolved mean flow, forcing the emergence of resolved flow structures in the regions where P_{SAS} is active. Since the sub-scale turbulence is adequately captured by using an advanced Reynolds-Stress Model, the spectral cut-off can be positioned more towards the low-frequency part of the spectrum, thus enabling coarser mesh resolutions. Exact mathematical formulation of P_{SAS} is non-unique and depends on the author's interpretation of Menter and Egorov's work. In this case, a simple relation promoting a stable solution process is being adopted in the form depending dominantly on the second derivative of the underlying velocity field $\nabla^2 U$:

$$P_{SAS} = C_1 \; max(\sqrt{k} \nabla^2 U - C_2 T_2, 0)) \tag{3}$$

Here, the value of the second derivative leads to the very intuitive behaviour: in case the flow exhibits a strong streamline curvature, which can either be inherently present (as e.g. in separation and re-circulation zones as well as in secondary flow events) or externally inflicted (by e.g. super-imposing the artificial perturbation) magnitude of the second derivative of the velocity field will naturally increase. If the mesh is appropriate, second-derivative can be accurately reconstructed and the eddy-resolving capability of the model will be amplified by increasing the P_{SAS}. On the other hand, $\sqrt{k}$ serves as a safeguard, prohibiting excessive destruction of modeled turbulence. T_2 stems from the transformation of equation and is mainly activated only near the walls, thus returning the RANS solution in their vicinity. Calibration of all constants is performed in Maduta (2013).

$$T_2 = 3k max\left[\frac{1}{k^2}\nabla k^2, \frac{1}{\omega^2}\nabla \omega^2\right] \tag{4}$$

.

RESULTS

Geometry of the computational domain with applied boundary conditions are adopted in accordance with the LES study by Tunstall *et al.* (2016), with exception of handling the inflow turbulence. Namely, turbulence at the main inlet is mapped from the parallel-running precursor simulation in a straight pipe. Precursor simulation also serves as a good indication of required mesh resolution, which is optimized in sense of correct prediction of wall shear stress (see e.g. ΔU_τ). Applied metrics is given in Table 2.

Table 2. Meshing metrics

Δr^+	$\Delta\Theta^+$	ΔL^+	ΔU_τ [%]
$0.5 - 70$	70	210	2.51

The results of the first- and second order statistics are presented in Fig. 1, and compared with DNS data for circular pipes by Pirozzoli *et al.* (2021). Concerning the velocity profile, its predicted near-wall shape follows closely the reference, which is naturally expected since the value of wall-shear stress was predicted accurately. Past the distance of $y^+ \approx 100$, slight deviations are notable although the general agreement with the data is good. This deviation can be explained by analysing the profiles of second-moments, where again, in the vicinity of the wall, both the anisotropy of turbulence, as well as the overall level of turbulent kinetic energy are predicted correctly. However, in the zone further away from the wall, a certain deviation from the DNS data is pronounced, being at strongest with respect to the stream-wise Reynolds stress component. According to the original work of Maduta (2013), the model tends to dissipate residual turbulence almost completely far away from the wall, hence the general level of turbulence is lower than expected. In spite of their somewhat smaller magnitude, second moments do exhibit a positive influence on the resolved scales since the general trend is correctly predicted and the simulation conditions don't correspond to a 'coarse DNS'. Mesh resolution with similar characteristics as in precursor case is afterwards used in the main simulation. Total number of cells is approx. 7.8 millions, which represents a substantial saving compared to approx. 80 million cells used in the reference LES case.

After eliminating the initial transient, the simulation has been run up to the convergence of second order statistics. Contours of mean velocity field are given in Fig. 3. Since the branch flow possesses a significantly lower momentum, it is forced to separate at the leading edge of the junction, creating a 'reattached-jet' configuration. We recall the back-bending of the mean dividing streamline at the point of reattachment being the characteristic feature of the redistribution term in

Eq. (1) in conventional RANS closure models (see e.g., Hanjalic & Jakirlic (1998)), indicating that the near-wall region is strongly affected by the modeled turbulence. The overall size of this 'primary' separation bubble corresponds approximately to $2D_b$, which is in accordance with the reference data. Additionally, due to the presence of an adverse pressure gradient within the elbow, main stream exhibits the 'secondary' separation at the location corresponds to 55^o behind the elbow entrance. Interestingly enough, separation wake reattaches and separates once again directly downstream of the elbow, creating a third separation zone which will be of decisive interest for this case. It is still unclear whether this deviation from the experiment is caused by the boundary conditions, or by the model itself. A more detailed discussion of this flow feature will follow in the following.

Profiles of the mean streamwise velocity are plotted against the LES reference in Fig. 4. Again, it can be seen that the overall agreement is very good, with small deviations at position $7D_b$ upstream, stemming from the additional, third separation that has been described previously. Although the mean flow is pushed away from the wall immediately past the elbow exit, it quickly recovers and almost complete agreement with the data is reached $2D_b$ upstream of the junction. At all locations, the results related to the near wall zone shows a very high level of agreement with the LES data. This is especially pronounced immediately downstream of the junction where the complex flow conditions involving the separation bubble are met.

Due to the lower flow mass, mixing of cold and hot streams doesn't influence the temperature distribution on the outlet dominantly. Therefore, of primary interest for this work is the distribution of temperature fluctuations on the surrounding wall surface, since it will dictate the propagation of thermally induced fatigue in the material. Projection of RMS ('Root Mean Square') values of the temperature field on to the upper wall of the junction is presented in Fig. 5. Regions of high amplitudes are established immediately behind the junction and are correlated with the boundary of the mixing zone, due to the presence of high amplitude, low rank structures in the separation wake. As will be demonstrated later on, energetic flow structures which are advected from the elbow exhibit a strong oscillating behaviour, which is oriented perpendicularly towards the branch flow, and the intensity of the RMS temperature is strongly correlated with the correct capturing of mixing dynamics in the wake. Next to the two symmetric belt-shaped contours downstream the branch pipe, zones of the highest variance are found at the leading edge of the junction. Based on the authors' experience with similar cases, this flow feature can be attributed to to the branch stream. Consequently, the temperature field undergoes the high-amplitude, low frequency pulsations that is dictated by the incoming flow, hence its high variance. the poor mixing process between the two fluid streams, which promotes a suppression of the fluctuations perpendicularly

As shown in Fig. 6, due to the longitudinal streamline curvature, region of an outwardly directed pressure gradient forms in the elbow, forcing sunsequently the fluid in near-wall zone to flow towards the centre of the curvature. Secondary structures typical of those resembling the Dean vortices are formed and advected downstream. Due to the continuity condition, stagnation point forms on the inner wall and promotes the decceleration of the flow, which separates at around 55^o behind the elbow entrance. Mean position of the Dean vortices is slightly more spread in relation to the LES-reference and can be attributed to the uncertainties in boundary conditions since the curvature-based phenomena are highly pressure- and less model dependent. Temporal dynamics of the secondary flows can be investigated by using the snapshot POD (Proper Orthogonal Decomposition) analysis, as described in Weiss (2019). With changes in the representation basis, generic flow variable Ψ, representing either velocity or temperature, is decomposed into the sorted sum of spatially coherent structures $\Phi_i(\vec{x})$ with the corresponding time dynamics $a_i(t)$:

$$\Psi(\vec{x},t) = \Phi_0(\vec{x}) + \sum_{i=1}^{+\infty} \Phi_i(\vec{x}) a_i(t) \tag{5}$$

where $\Phi_0(\vec{x})$ represents the mean.

Visualisation of two most energetic modes $\Phi_1(\vec{x})$ and $\Phi_2(\vec{x})$ with their temporal dynamics at location $2D_m$ upstream of T-Junction is presented in Fig. 7. It can be seen that the switching frequency of the dominant vortex pair corresponds roughly with $St \approx 0.21$ which is in accordance with reference data. However, a second frequency peak, non-existent in the reference, with switching frequency of $St \approx 0.5$ appears in the frequency signature as well. There are many possible reasons causing this behaviour, from uncertainties in boundary conditions (e.g., the pressure field is directly mapped from the precursor simulation) to the intrinsic behaviour of the model. We speculate that this additional vortex pair stems primarily from the secondary flow appearance formed in additional (third) separation zone at the elbow exit. Since the separation zone is confined by the presence of the Dean vortex pair, it is expected that the switching frequency will be increased. However, since the energy is primarily attained at $St \approx 0.21$, we conclude that the behaviour of the flow is less dependent of the pressure boundary conditions and is more a model-related problem.

Further downstream, at the position $1D_b$ behind the junction, this additional separation wake evolves in a more complex structure, with several higher harmonics in the range between $St \approx 0.1$ and $St \approx 1.0$. Spatially, three distinct zones of horizontally oriented vortex switching directions are identified in Fig. 8, stemming from the elbow-related Dean vortex pair, junction-related separation bubble vortices and third separation wake from the elbow exit. Despite correctly reproducing the natural frequency response of the vortex switching, which is dictated by the pressure-related phenomena, it seems that the Dean vortex pair together with the elbow wake exhibits multiple contractions and expansions along the downstream coordinate, which would explain higher harmonics in the data. Due to the incapability of the POD method to discriminate between separate frequencies for a given mode, it was not clear what physical phenomenon is correlated with the frequency peaks. Therefore, we additionally analyse the temperature field to correlate the temperature switching frequency with the underlying flow structure.

The POD analysis of the temperature field $1D_b$ behind the junction is given in Fig. 9. As for the most energetic POD mode, the principal directions of temperature pulsations are oriented, as expected, perpendicularly to both the direction of the branch flow, as well as the curvature radius. Although the frequency signature of $St \approx 0.21$, originating from the Dean vortex pair, is present in the signal, it doesn't decisively influence the temperature pulsations. Dominant peak of $St \approx 0.5$ shows that thermal mixing in the junction is dictated mostly by the dynamics of the additional separation wake, formed at the elbow exit. Although the natural switching frequency of the separation bubble is expected to lie around $St \approx 0.1$, it is somehow obscured by the dynamics of the more energetic inflow flow structures, and can not be distinguished in the signal. The second POD mode seems to be non-symmetrical in regard to the vertical coordinate, and stems from the separation of the branch flow at the trailing edge of the junction, which produces pulsations in the temperature field at the edge of the mixing wake.

CONCLUSION

Thermal mixing of two fluid streams at a moderately high Reynolds number has been simulated by using the scale-adaptive computational strategy. Correspondingly sensitized differential Reynolds-Stress Model is utilized to describe the dynamics of the sub-scale turbulence. Substantial saving regarding the computational effort has been achieved in comparison with the reference LES case. The flow statistics has been predicted following closely the LES reference, showing the capability of the model to reproduce complex flow conditions at reasonable costs. Considering the temporal dynamics of the mixing structures, the Proper-Orthogonal-Decomposition analysis has been perfoemd to analyze temporal response of the most energetic flow features. Due to the strong influence of pressure-driven effects, the dynamics of an elbow-induced Dean vortex pair has been adequately reconstructed by the model. However, at elbow exit, another flow separation occurs, injecting additional peaks into the eddy-switching spectrum. Source of this additional separation zone remains likely model-related. This third separation wake is retained in the vicinity of the upper wall and has affecting decisively the dynamics of the mixing structures, which is no longer dominantly influenced by the Dean vortex pair at $St \approx 0.21$, but by the dynamics of the vortex pair, present in the third separation zone, at $St \approx 0.5$.

Acknowledgment Financial support from the German Academic Exchange Service (DAAD - Deutscher Akademischer Austauschdienst) is gratefully acknowledged.

REFERENCES

Hanjalic, K & Jakirlic, S 1998 Contribution towards the second-moment closure modelling of separating turbulent flows. *Computers and Fluids* **27** (2), 137–156.

Hosseini, S. M., Yuki, K. & Hashizume, H. 2008 Classification of turbulent jets in a T-junction area with a 90-deg bend upstream. *Int. J. Heat and Mass Transfer* **51**, 2444–2454.

Jakirlic, S. & Hanjalic, K. 2002 A new approach to modelling near-wall turbulence energy and stress dissipation. *Journal of Fluid Mechanics* **459**, 139–166.

Jakirlic, S. & Maduta, R. 2015 Extending the bounds of 'steady' RANS closures: Toward an instability-sensitive Reynolds stress model. *Int. J. Heat and Fluid Flow* **51**, 175–194.

Maduta, R. 2013 An eddy-resolving Reynolds stress model for unsteady flow computations: development and application. PhD thesis, Technische Universität Darmstadt, Darmstadt, Germany.

Menter, F. & Egorov, Y. 2010 The scale-adaptive simulation method for unsteady turbulent flow predictions. Part 1: theory and model description. *Flow, Turbulence and Combustion* **85**, 113–138.

Pirozzoli, S., Romero, J., Fatica, M., Verzicco, R. & Orlandi, P. 2021 One-point statistics for turbulent pipe flow up to $Re_\tau \approx 6000$. *Journal of Fluid Mechanics* **926**, 355–377.

Tunstall, R., Laurence, D., Prosser, R. & Skillen, A. 2016 Large eddy simulation of a T-junction with upstream elbow: The role of Dean vortices in thermal fatigue. *Applied Thermal Engineering* **107**, 672–680.

Weiss, Julien 2019 A tutorial on the Proper Orthogonal Decomposition. *AIAA Paper 2019-3333* .

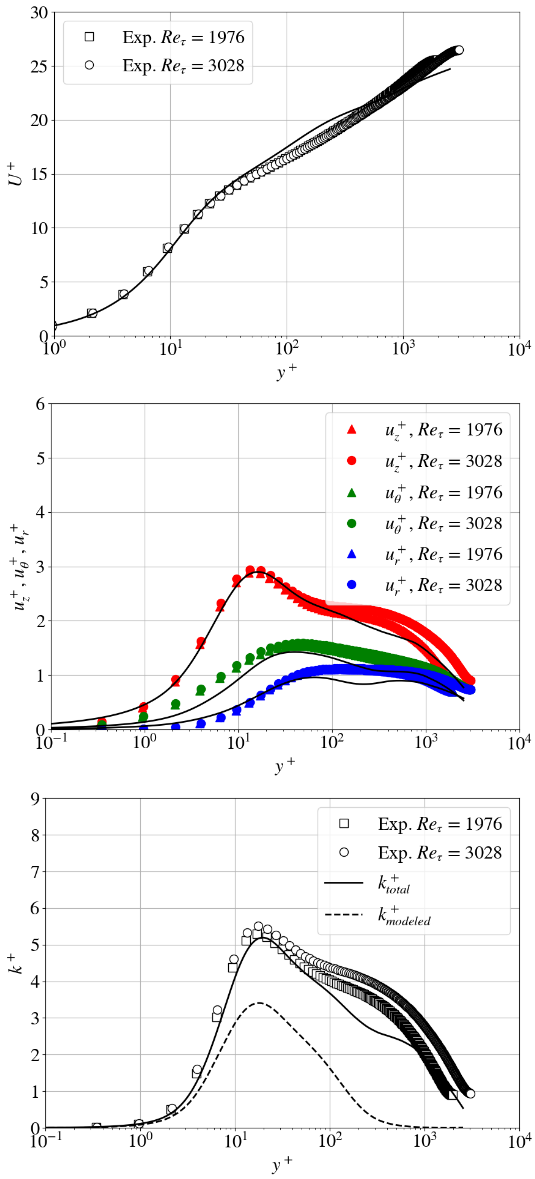

Figure 1. Validation of the precursor pipe flow simulation : profiles of the mean-velocity (upper), normal Reynolds stress components (middle) and turbulence kinetic energy (lower).

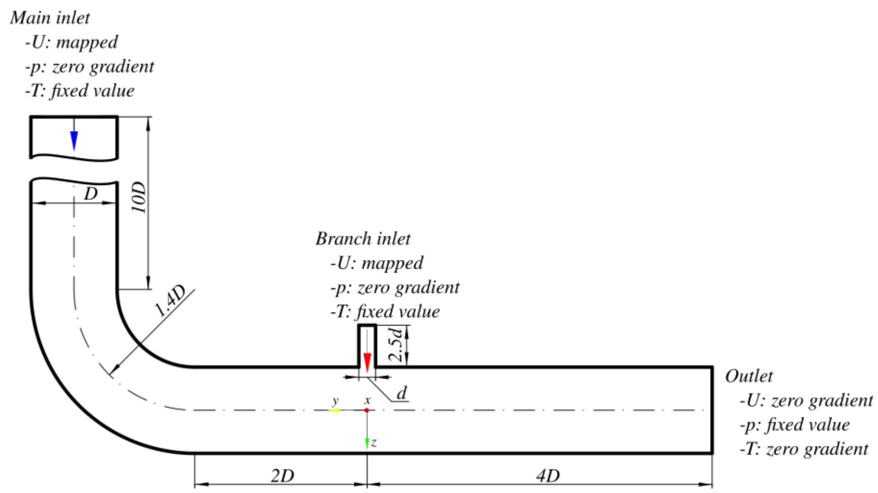

Figure 2. Schematic of the solution domain with assigned boundary conditions.

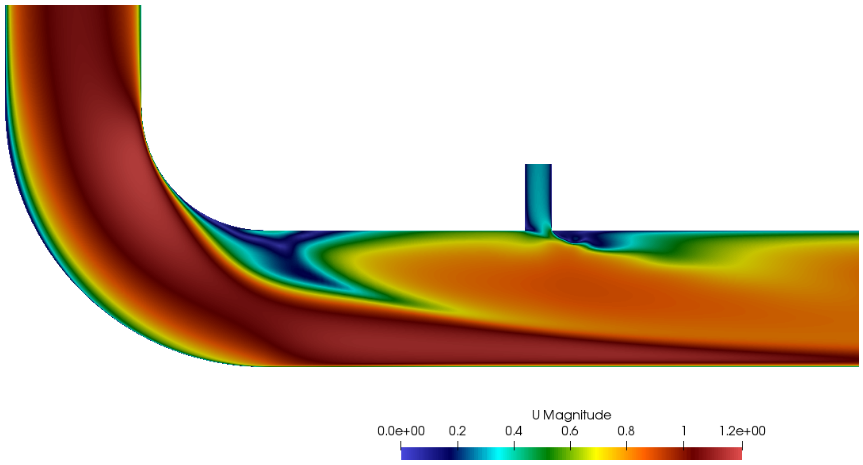

Figure 3. Contours of the mean velocity field, colored by its magnitude. Note that the figure is not in scale with the schematic.

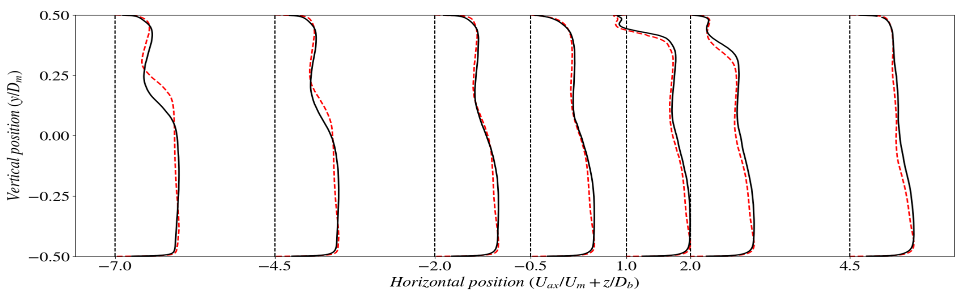

Figure 4. Profiles of the streamwise velocity. Reference data from LES study are given in red dashed lines.

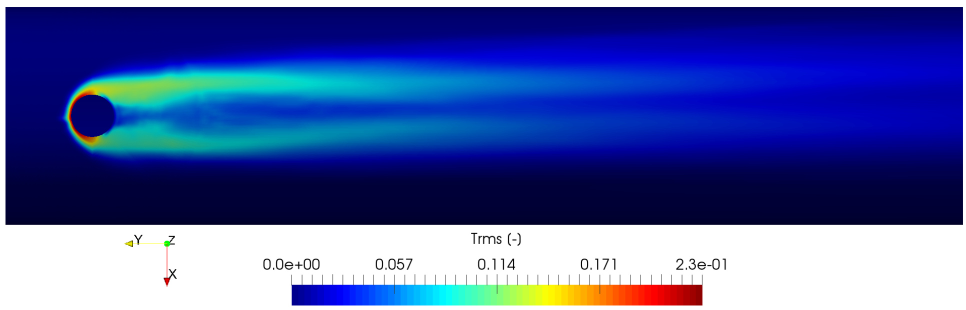

Figure 5. Contours of the dimensionless RMS Temperature on the upper wall.

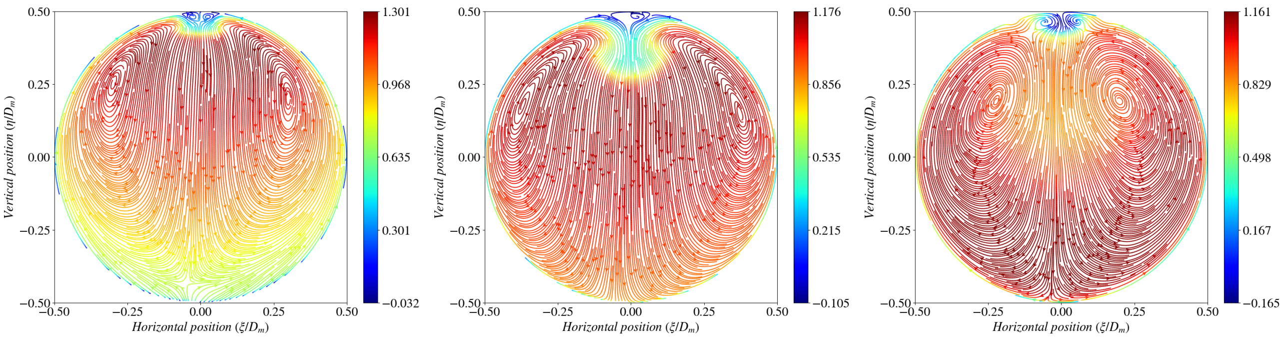

Figure 6. Streamlines of the secondary flow, respectively at locations 65^o (left) and 90^o (middle) behind the elbow entrance, as well as $1D_b$ (right) behind the junction. Backward coloring corresponds to the magnitude of the streamwise velocity component.

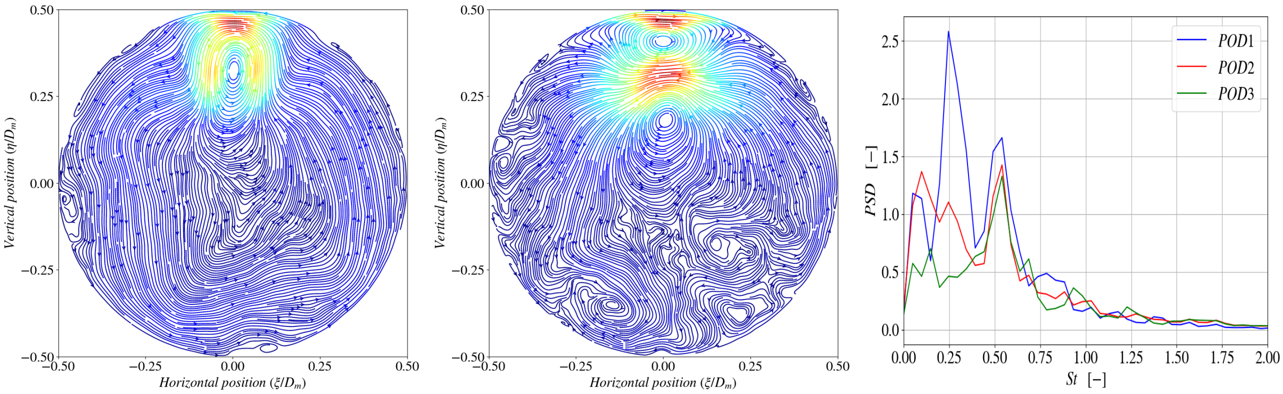

Figure 7. Streamlines of the first (left) and second (middle) most dominant POD mode of the velocity field at location $2D_m$ upstream of the junction, with the FFT Analysis of their time coefficient (right). Backward coloring indicates the magnitude of the mode.

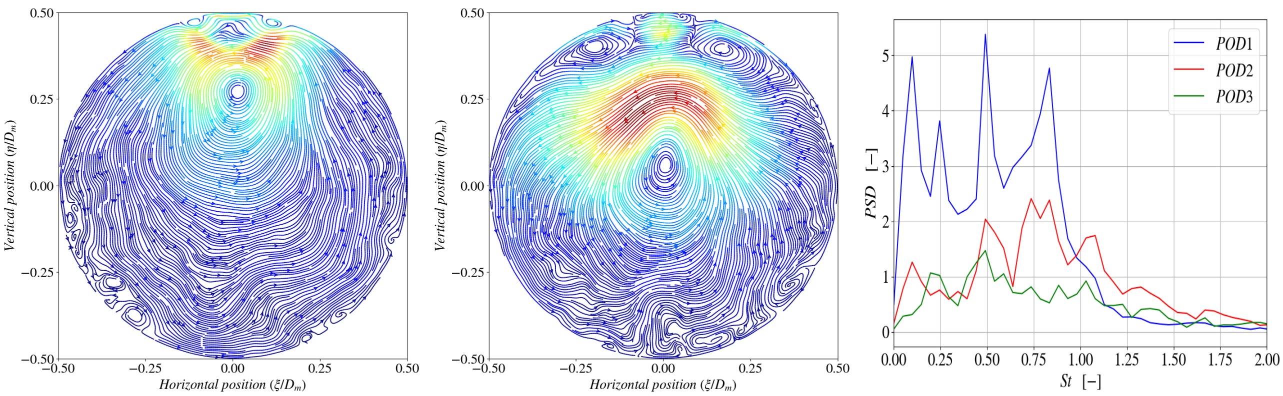

Figure 8. Streamlines of the first (left) and second (middle) most dominant POD mode of the velocity field at location $1D_b$ downstream of the junction, with the FFT Analysis of their time coefficient (right). Backward coloring indicates the magnitude of the mode.

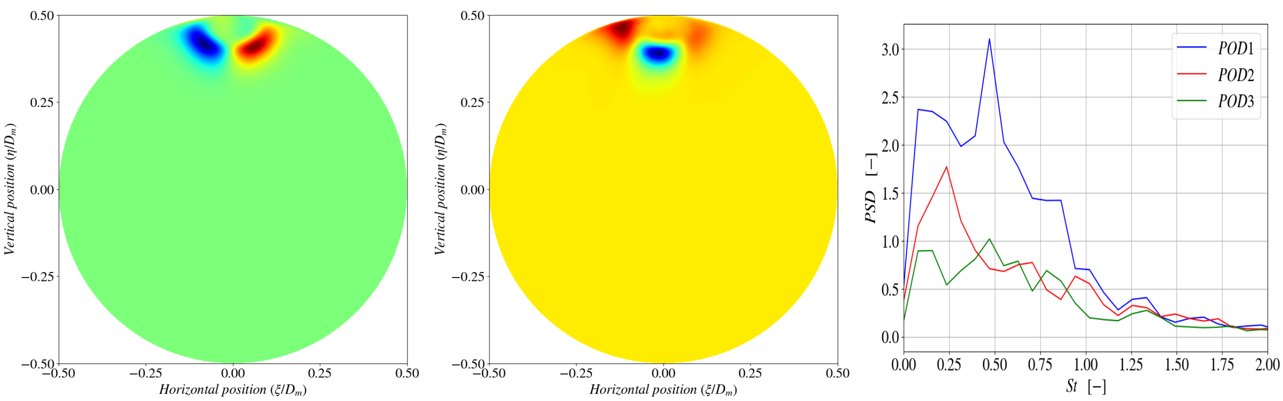

Figure 9. Contours of the first (left) and second (middle) most dominant POD mode of the temperature field at location $1D_b$ downstream of the junction, with the FFT Analysis of their time coefficient (right). Backward coloring indicates the magnitude of the mode.